



# Material mapping strategy to identify the density-dependent properties of dry natural snow

Hassan Bahaloo<sup>1</sup> · Fredrik Forsberg<sup>1</sup> · Henrik Lycksam<sup>1</sup> · Johan Casselgren<sup>1</sup> · Mikael Sjö Dahl<sup>1</sup>

Received: 11 November 2023 / Accepted: 7 January 2024 / Published online: 31 January 2024  
© The Author(s) 2024

## Abstract

The mechanical properties of natural snow play a crucial role in understanding glaciers, avalanches, polar regions, and snow-related constructions. Research has concentrated on how the mechanical properties of snow vary, primarily with its density; the integration of cutting-edge techniques like micro-tomography with traditional loading methods can enhance our comprehension of these properties in natural snow. This study employs  $\mu$ CT imaging and uniaxial compression tests, along with the Digital Volume Correlation (DVC) to investigate the density-dependent material properties of natural snow. The data from two snow samples, one initially non-compressed (test 1) and the other initially compressed (test 2), were fed into Burger's viscoelastic model to estimate the material properties.  $\mu$ CT imaging with 801 projections captures the three-dimensional structure of the snow initially and after each loading step at  $-18^{\circ}\text{C}$ , using a constant deformation rate (0.2 mm/min). The relative density of the snow, ranging from 0.175 to 0.39 (equivalent to 160–360 kg/m<sup>3</sup>), is determined at each load step through binary image segmentation. Modulus and viscosity terms, estimated from Burger's model, exhibit a density-dependent increase. Maxwell and Kelvin–Voigt moduli range from 0.5 to 14 MPa and 0.1 to 0.8 MPa, respectively. Viscosity values for the Maxwell and Kelvin–Voigt models vary from 0.2 to 2.9 GPa-s and 0.2 to 2.3 GPa-s within the considered density range, showing an exponent between 3 and 4 when represented as power functions. Initial grain characteristics for tests 1 and 2, obtained through image segmentation, reveal an average Specific Surface Area (SSA) of around 55 1/mm and 40 1/mm, respectively. The full-field strain distribution in the specimen at each load step is calculated using the DVC, highlighting strong strain localization indicative of non-homogeneous behavior in natural snow. These findings not only contribute to our understanding of natural snow mechanics but also hold implications for applications in fields such as glacier dynamics and avalanche prediction.

**Keywords** Material mapping · Micro tomography · Compression test · Digital volume correlation · Snow and ice

## 1 Introduction

Snow is a complex material that, in addition to being viscous and plastic, undergoes volume changes, or density variations, under compressive loading. The intricate structure of snow particles further adds to this complexity, with micro-level arrangements strongly influenced by factors such as temperature and super-saturation [17].

Extensive research has been conducted on snow due to its significance in various aspects of human life, as evident in studies by [6–8, 10, 12, 15, 18, 20, 22, 25, 30, 31, 33–36].

Comprehensive reviews on snow mechanics can be found in [19, 23, 27].

Mechanical properties of snow are often reported as a function of density [19]. While Young's modulus is commonly used, the viscous behavior of snow is also investigated [16, 19, 26, 28, 31]. The viscoelastic behavior is typically modeled using the Burgers model, consisting of Voigt units in series with Maxwell units [14], widely applied in the analysis and design of viscoelastic materials [4, 9, 21]. Density-dependent material properties of snow are modeled using either power law [32] or exponential law [13].

The strain rate significantly affects snow's mechanical behavior as a rate-dependent material [19]. Delineating loading rates is crucial, with quasi-static loading rates ( $\dot{\epsilon} \approx 10^{-3}$  1/s) and dynamic regimes ( $\dot{\epsilon} > \times 10^{-2}$  1/s) showing distinct mechanical responses [24, 29].

✉ Hassan Bahaloo  
hassan.bahaloo@ltu.se

<sup>1</sup> Division of Experimental Mechanics, Luleå University of Technology, Luleå, Sweden

Utilizing the visco-elastic nature of snow, step-wise loading combined with  $\mu$ CT allows for identifying material properties by considering creep and relaxation [13]. Despite challenges in sample sizes for  $\mu$ CT investigations, with a size greater than 9 mm ensuring size-independent results [8], linking  $\mu$ CT to mechanical loading enables detailed Finite Element Method (FEM) analysis [25], exploration of micro-structural changes and mass transfer [20, 33], and estimation of elastic modulus [7, 30, 34]. Additionally, advanced techniques like Digital Volume Correlation (DVC) applied to  $\mu$ CT scans effectively calculate 3D displacement fields within snow samples [10]. The study by [10] made no effort in identifying the material properties of snow based on the observed stress response. The study of natural snow for real-life applications required precise knowledge about the variations in mechanical properties like stiffness and viscosity with density.

In our previous study [1], we explored the subject of material mapping for the manufactured snow as a function of its density under quasi-static loading. This paper focuses on the analysis of dry natural snow, utilizing  $\mu$ CT imaging and mechanical loading to assess the applicability of the Burgers model in capturing density-dependent material properties. Micro-CT imaging provides insights into density distribution during deformation, enhancing our ability to model material behavior and extending our investigation to natural snow. The subsequent sections provide a concise literature review and motivation (Sect. 1), detailed materials and methods (Sect. 2), study methods (Sect. 3), and thorough discussions on implications and limitations (Sect. 4).

## 2 Materials and methods

The experimental procedure is outlined elsewhere [1] in detail for the case of manufactured snow. The schematic with slight changes appears in Fig. 1. The same methodology,

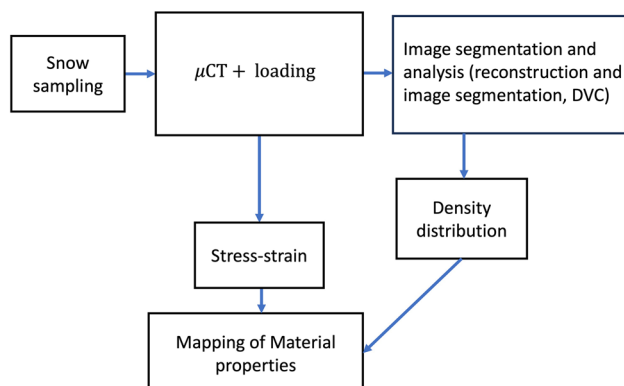


**Fig. 1** Schematic of the steps conducted to obtain density resolved material properties of dry snow

which will be outlined in the following sub-sections, is used in this study as in the study on manufactured (artificial) snow as described in [1]. In short, we have conducted experiments on two snow samples and refer to them as “test 1” and “test 2”. In test 1, the snow is filled in the tube without any external compressing force. In test 2, a mild compressing force is applied on the snow pack in the tube to achieve a range of higher densities. The block named “snow sampling” in Fig. 1 refers to either of test 1 or 2. This process is further detailed in Sect. 2.1. The middle column blocks represent the measurement, which is performed in a micro-tomography X-ray machine ( $\mu$ CT). During measurements, the snow sample is kept at a constant temperature and compressed uniaxially in small steps while monitoring the force response. At each compression level, the sample is held for a specific duration to allow for relaxation, and subsequently, the structure is recorded by the CT machine. The relaxation time was decided by CT operator when the changes in the observer force output from the load cell becomes low enough that the subsequent imaging could be conducted without artifacts. With this approach, we have access to both the time-resolved force response and the density distribution at each compression level, which serve as inputs for further analysis. The entire procedure is detailed in Sect. 2.2. The right part of Fig. 1 represents the analyses that are performed on the data provided by the experiments and are detailed in Sect. 2.3. The force response acquired is fitted to a viscoelastic model known as Burger’s model, which includes two stiffness terms and two viscosity terms, respectively. After reconstruction, the  $\mu$ CT data are segmented, providing the volume fraction of snow at each load step. These volume images are used in two ways. The first use is to calculate the average density to be connected with the calculated material parameters. The other use is to calculate the distribution of strain by applying a Digital Volume Correlation (DVC) algorithm. The main purpose of this last step is to make sure that the deformation induced on the snow sample is uniaxial and uniform. The entire procedure is outlined in the following sections.

### 2.1 Snow sampling

Freshly precipitated snow was collected at Luleå University of Technology, Luleå, Sweden, on December 19th, 2022, at approximately 10 a.m. from the snowfall of the night before. The temperature during the sample collection was  $-8^{\circ}\text{C}$  and the relative humidity of the air was 88%.

Snow was sampled from the containers and placed into Polymethyl methacrylate (PMMA) tubes having an internal diameter of 9 mm, wall thickness of 1 mm, and a height of 11 mm. An aluminum plate was placed at the bottom of the PMMA tube to enhance heat transfer, as explained in [1]. The sampling process involved inserting the PMMA tubes into the snow inside the containers. The excess snow

on top of the PMMA tube was carefully removed by gently shearing it away with a cold glass plate without applying pressure. Finally, an aluminum punch with a diameter of 9 mm and a height of 5 mm was carefully placed on top of the snow sample before mounting it on the movable punch. During the entire handling and sampling process, extra caution was taken to prevent any contact with warm surfaces in order to avoid rapid crystallization that could initiate from the container walls. As mentioned earlier, two snow samples were collected: one without any external pressure during the filling (test 1), and the other with some external pressure to obtain higher densities (test 2).

## 2.2 Micro CT imaging and testing

Figure 2 illustrates the snow sample and its positioning in the  $\mu$ CT machine. Specific elements in the environment

$$\sigma(t) = \frac{k_1}{m_1 - m_2} \left\{ E_M(e^{m_1 t} - e^{m_2 t}) + \eta_M(m_2 e^{m_1 t} - m_1 e^{m_2 t}) + \eta_M \right\} - \frac{k_1 \hat{H}(t - t_l)}{m_1 - m_2} \left\{ E_M[e^{m_1(t-t_l)} - e^{m_2(t-t_l)}] + \eta_M[m_2 e^{m_1(t-t_l)} - m_1 e^{m_2(t-t_l)}] + \eta_M \right\}, \quad (1)$$

are labeled from 1 to 5, while details of the snow sample mounted on the punch are indicated as numbers 6–8. The  $\mu$ CT system utilized in this study was the ZEISS Xradia 620 Versa, consisting of a sealed microfocus X-ray tube, a 4-axis sample stage, and a high-resolution detector, all mounted on a stable granite block. To facilitate controlled loading and displacement measurement in a temperature-controlled setting, an in-situ load stage (CT5000TEC, Deben UK Limited, Bury Saint Edmunds, UK) with a 500 N load cell was integrated into the system.

All experiments were conducted at a temperature of  $-18^\circ\text{C}$ . The sample underwent displacement-controlled loading, with a total compression of nearly 4 mm for test 1 and nearly 2.2 mm for test 2. The loading speed was set at

0.2 mm/min. Considering the sample height of 7.5 mm at the beginning of the compression, the corresponding strain rate is  $4.4 \times 10^{-4} \text{1/s}$ . After reaching each plateau, the sample was allowed to relax until the differences in the observed force level on the screen were decided in such a way that the consequent imaging became artifact-free. The force was continuously recorded and then divided by the inner cross-sectional area of the tube to determine the average stress applied to the sample.

## 2.3 Analysis

Snow is a viscous material [19] which may be modeled using the Burger's model presented in Fig. 3. When applying a pulse of strain rate,  $\dot{\epsilon} = k_1 [\hat{H}(t) - \hat{H}(t - t_l)]$ , where  $k_1 = 2 \text{ mm/min}$  is the strain rate applied during loading, and  $\hat{H}(t)$  is the Heaviside step function, the resulting stress response can be obtained as follows using the Burger's model [1]:

with  $m_1$  and  $m_2$  defined in [1] and  $t_l$  is the duration of loading for each loading step, which is the time from the start of the deformation-controlled test.

A discrete minimum search at a selected times,  $t_i$ , is conducted according to [1] to find the material properties that minimize  $[\sigma(t_i) - \hat{\sigma}(t_i)]^2$ , where,  $\sigma$  and  $\hat{\sigma}$  are measured stress and estimated stress using Eq. (1), respectively.

The software utilized for managing and segmenting the tomographic images provided by the system is Dragonfly (ORS, Montreal, Canada). One of the key manipulations performed on the images is binary segmentation, which involves dividing the image into two categories: “white” representing snow and “black” representing air. This

**Fig. 2** Experimental setup: (Left) the experimental environment; (Right) the snow sample mounted on the punch. Numerated items: 1:  $\mu$ CT source 2: temperature-controlled in-situ load stage 3: Granite base 4: Magnification-tunable detector with  $2\text{k} \times 2\text{k}$  16 bit CCD camera 5: 4-axis, motorized precision sample stage 6: Fixed punch 7: PMMA tube containing ice 8: Movable punch [1]

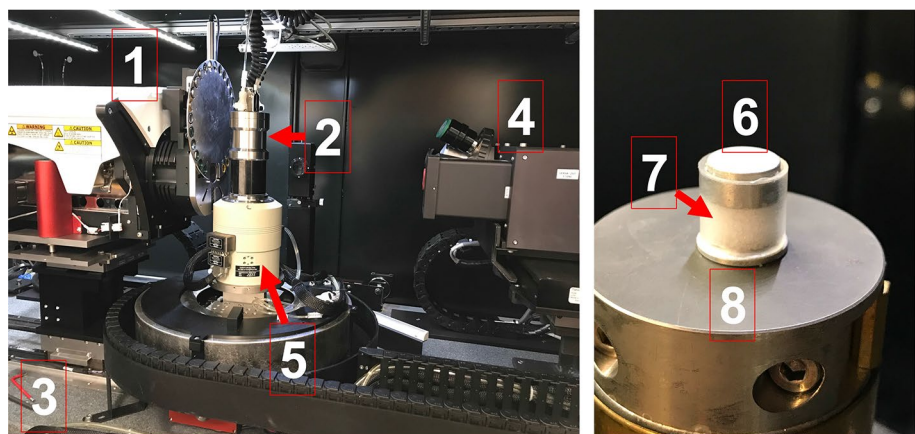
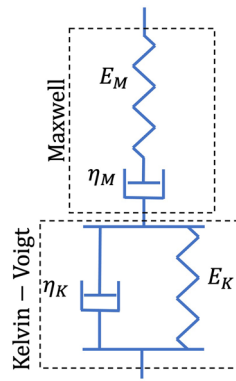


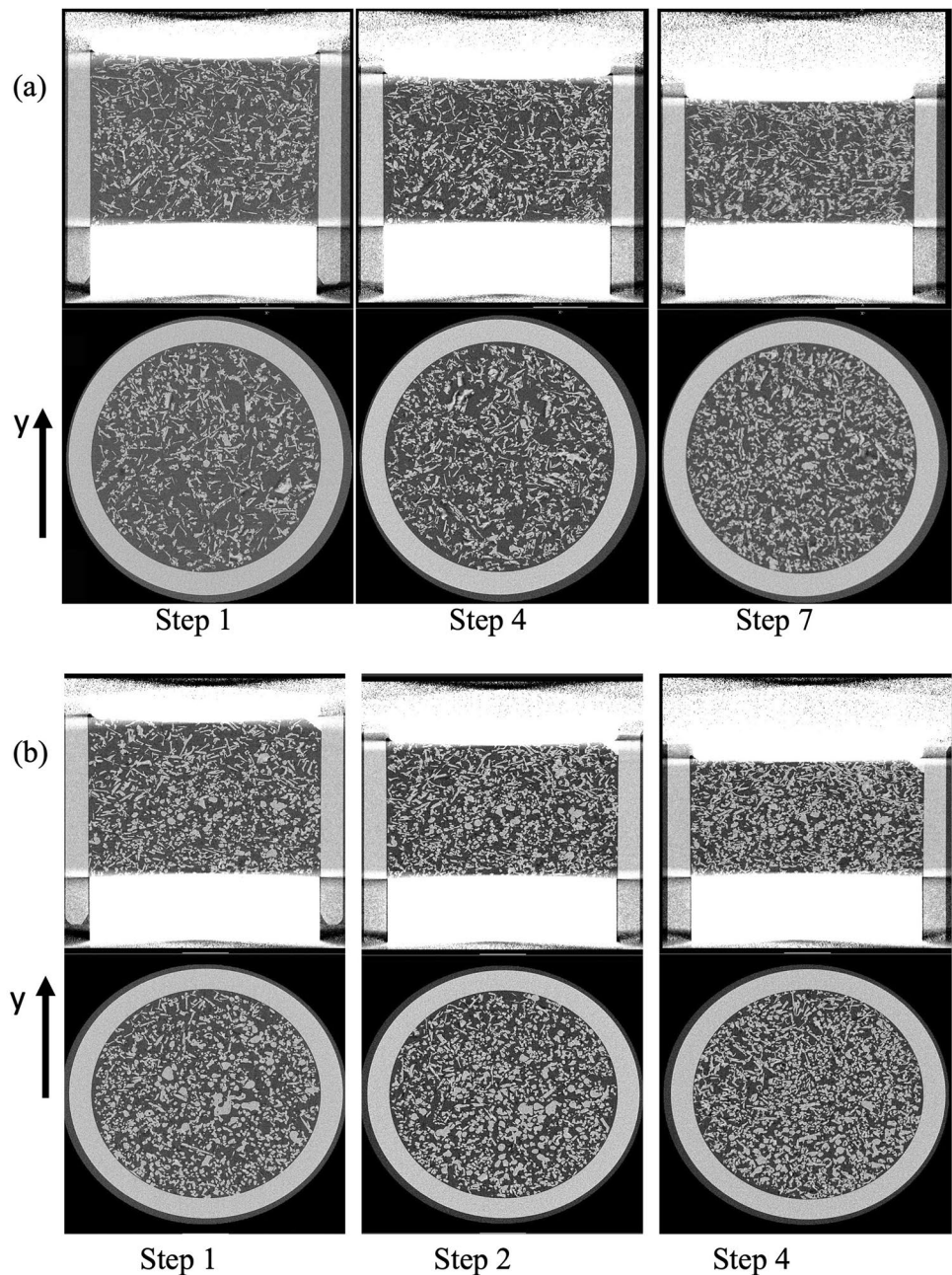
**Fig. 3** Burger's model for visco-elastic material. It is a combination of Maxwell and Kelvin–Voigt model in series.  $E_M$  and  $\eta_M$  the stiffness and viscosity of the Maxwell model, respectively.  $E_K$  and  $\eta_K$  the stiffness and viscosity of the Kelvin–Voigt model, respectively



segmentation enables the extraction of particle properties like specific surface areas, as depicted in Fig. 6. Additionally, the relative density is calculated by dividing the number of black pixels by the total number of pixels in the image. The calculations were carried out using Matlab (v 2022a, Mathworks, MA).

To obtain the relative density of a specific axial segment, the number of white pixels in that slice is counted and compared to the total number of pixels. By multiplying this value by the density of ice ( $\rho = 0.917 \text{ g/cm}^3$ ), the true density can be determined.

**Fig. 4** Sample CT images during the loading of the snow specimen **a** test 1: step 1, 4, and 7 (final) and **b** test 2: steps 1, 2, and 4 (final)



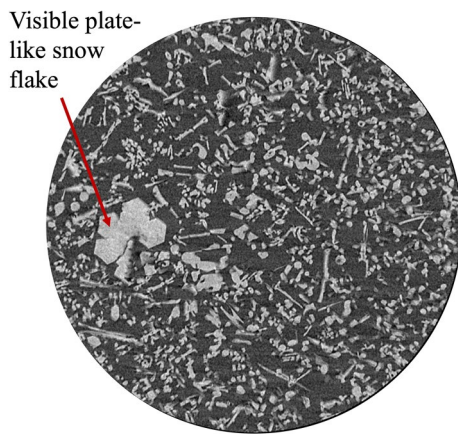


**Fig. 5** A visible plate-like snow flake taken from a horizontal cross section in the middle of the height of the snow sample in the beginning of the loading for test 1

The DVC is employed to obtain full-field displacements of snow, and the axial component of the strain fields are then computed through differentiation. DVC tracks the movements of small volumes in the system during loading and estimates the displacement fields at each time step using correlation methods. A detailed explanation of the DVC technique can be found in [3, 5, 11]. The DVC analysis was conducted using LaVision Davis 8.4 from LaVision Inc., located in Ypsilanti, MI, USA. The approach utilized a multi-grid differential correlation approach with a final sub-volume size of  $32 \times 32 \times 32$  voxels and 75% overlap.

### 3 Results

Cross-sections of the 3D structure of the snow sample for tests 1 and 2 are shown at different load steps in Fig. 4a and b, respectively. The particles are a combination of the needles and plate-like snowflakes. The compression direction is indicated as “y” in the image, and the loading step

increases from left to right. Snow particles have complex and varied shapes with a combination of needle- or plate-like flakes. A visible hexagonal plate-like snow flake from the sample related to test 1 in the middle axial axis is presented in Fig. 5.

Particle characteristics for tests 1 and 2 are more detailed in Fig. 6. The total number of particles is around 7000 and 9000 for tests 1 and 2, respectively. The histogram of the volumes of particles decreases rapidly, and most particles have volumes less than  $0.01 \text{ mm}^3$ . The same trend is observed for the histogram of the surface area of the particles, and most particles have a surface area less than  $0.5 \text{ mm}^2$ . The SSA of the particles has a mode around 55  $1/\text{mm}$  and 40  $1/\text{mm}$  for tests 1 and 2, respectively.

From Fig. 4, it is visually seen that the density increases as the punch pushes deeper into the sample. The calculated distributions of the density at different load steps presented in Fig. 7 show that the density is not varying significantly with the height of the cylinder, but the variations are more pronounced when compared to the case of the manufactured snow in our previous work, [1]. The density increases with the loading sequence, which is expected since the snow is being compressed.

As part of a further investigation into the uniformity of compaction, a cross section of the axial strain in the loading direction, obtained from the DVC is presented in Fig. 8 and Fig. 9, respectively. The overall axial strain value increases to around 0.33 and 0.25 for test 1 and test 2, respectively. Moreover, the strains exhibit localization behavior which is a characteristic of granular materials. The localization of the strain is much more pronounced than our previous results for the case of manufactured snow [1].

The most important result that is used to estimate the material properties is the stress–time response. The nominal compressive stress,  $\sigma = F/A$ , (where  $F$  is the applied force and  $A$  is the cross section of the PMMA tube), is plotted as a function of the nominal strain,  $\epsilon = \delta/L$  (where  $\delta$  is the imposed displacement and  $L$  is the height of the PMMA

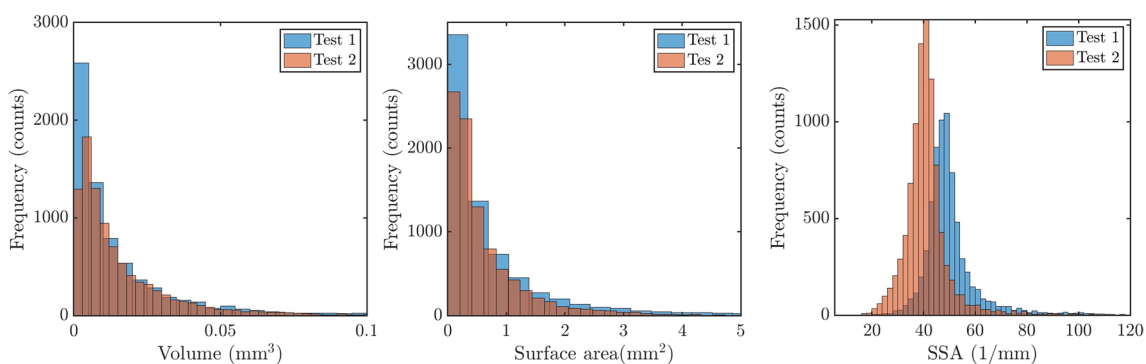


**Fig. 6** Histograms of the volume of the particles, surface area, and SSA for test 1 and 2; total number of particles: 7000 and 9000 for test 1 and 2, respectively

**Fig. 7** Density variation in axial and radial segments, respectively. Each of the shown curves represents the density value at the specific layer of image pixels, which represents the relative axial position. For a specific load step, at each axial position, there are values of density indicating the average value in one quarter of the cross section at that axial position

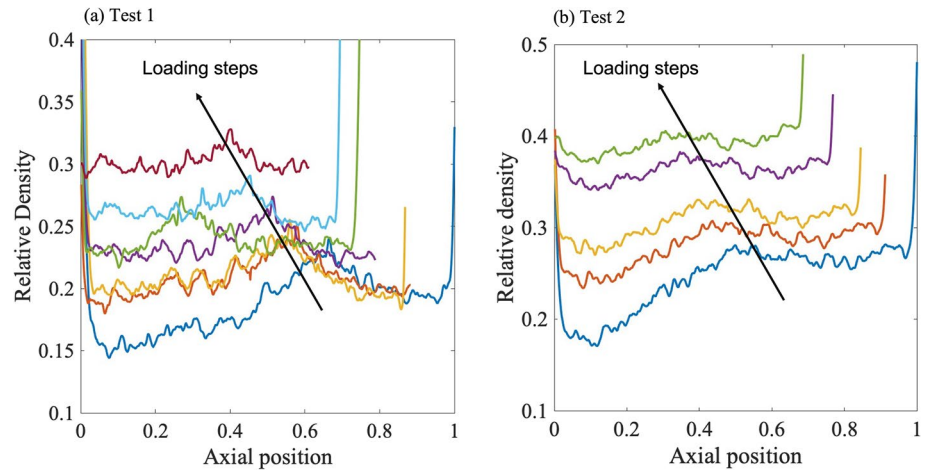


**Fig. 8** Axial strain distribution obtained from the DVC for test 1. The original height of the snow at the beginning of the compression was 7.5 mm. The imposed nominal strain is indicated at the top of each image. The dark blue color shows the minimum strain, while the red color is the strain near zero

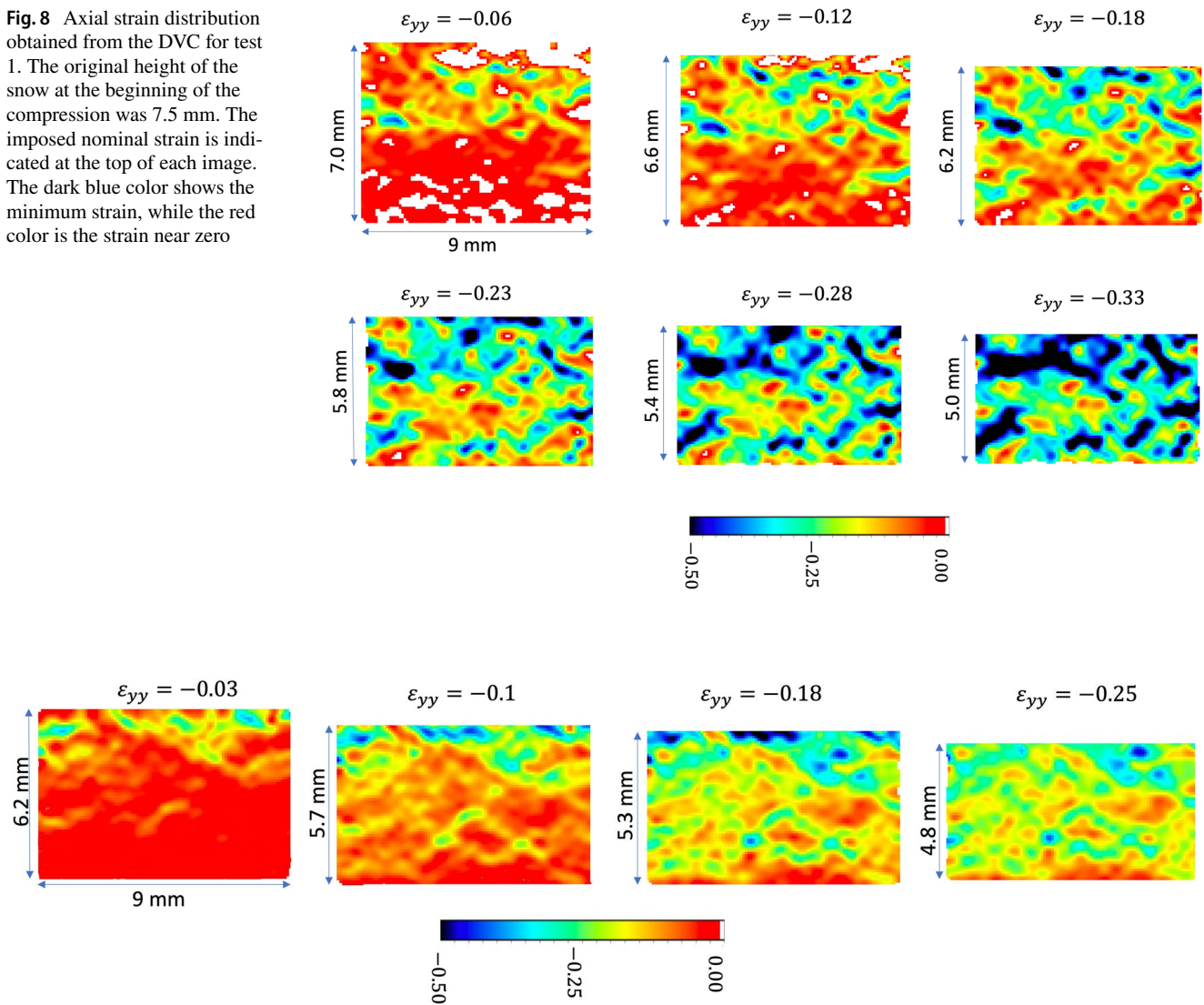


**Fig. 9** Axial strain distribution obtained from the DVC for test 2. The original height of the snow at the beginning of the compression is 6.4 mm. The imposed nominal strain is indicated at the top of each

image. The dark blue color shows the minimum strain, while the red color is the strain near zero

**Fig. 10** Stress–strain and stress–time responses for tests 1 and 2. W1 and W2 show focused view windows of one sample peak of stress–time for test 1 and test 2, respectively. In both W1 and W2, the creep relaxation behavior of snow is visible. The drops in the stress–strain curve correspond to the relaxations

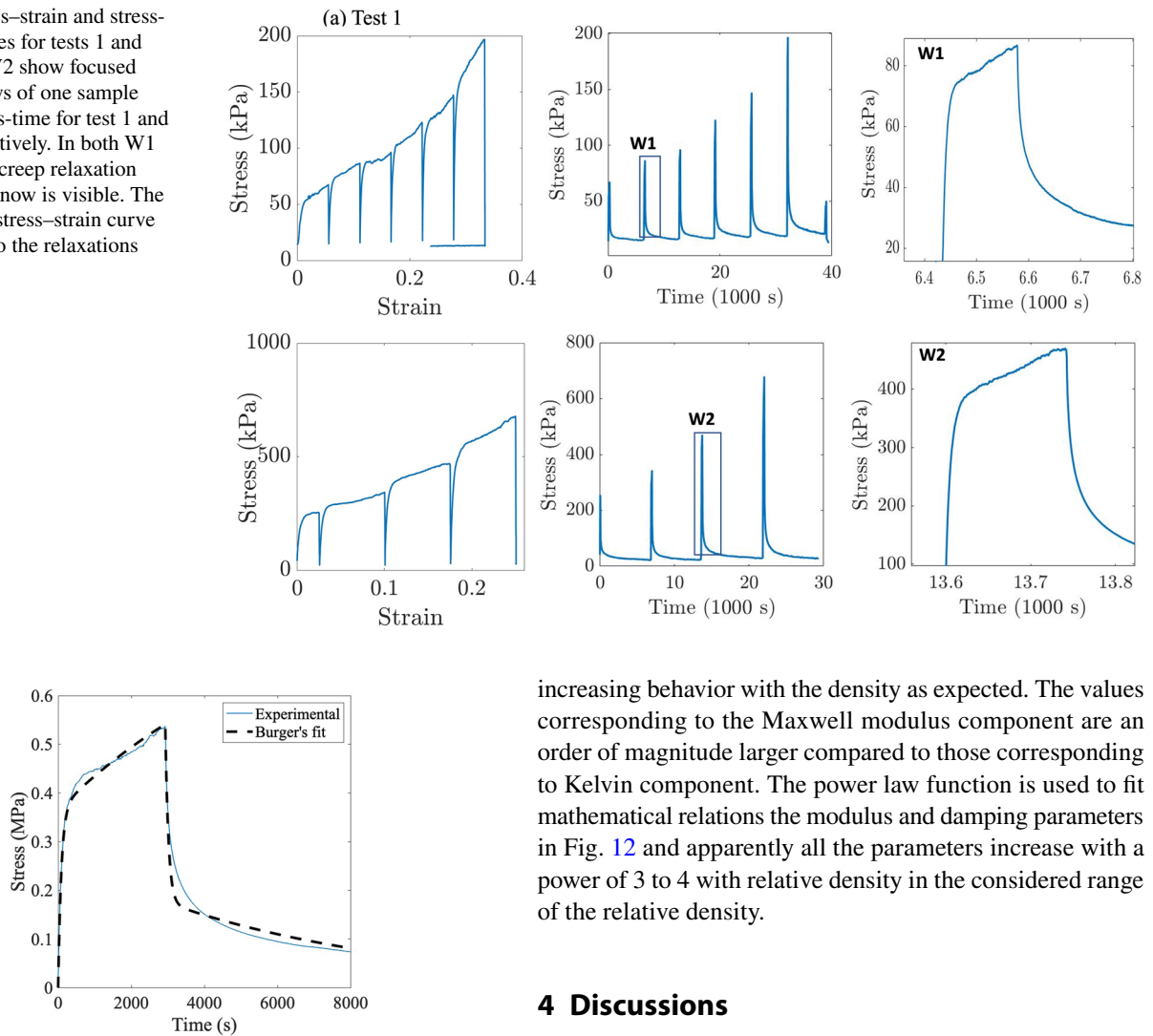


**Fig. 11** Sample curves fitted to the last step of stress–time response of test 2 using Eq. (1)

tube) in Fig. 10. Stress increases during loading and quickly decreases due to relaxation after the loading is stopped. The stress–time plot is presented in Fig. 10 with windows w1 and w2 depicting a more detailed nature of relaxation behavior for a specific loading step for test 1 and test 2, respectively. The combined creep–relaxation that appears at each loading step defines the viscoelastic behavior at the corresponding level of compaction, a behavior that can also be described by Eq. (1). As an example, Fig. 11 shows the last loading step for test 2 along with the fitted results using the Eq. (1). Then, for each level of compaction, the four material parameters of interest are retrieved.

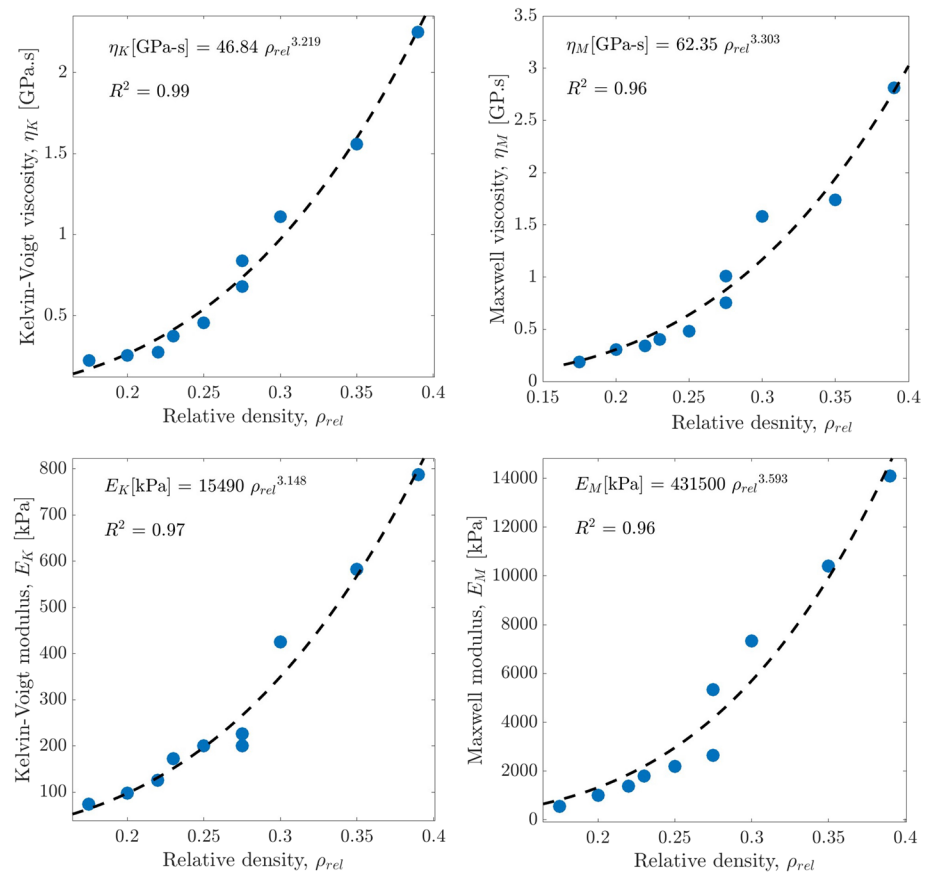
Finally, the four parameters corresponding to the stiffness and damping (modulus and viscosity interchangeably) of the snow are plotted against relative average density in Fig. 12. All the damping and the modulus parameters indicate an

increasing behavior with the density as expected. The values corresponding to the Maxwell modulus component are an order of magnitude larger compared to those corresponding to Kelvin component. The power law function is used to fit mathematical relations the modulus and damping parameters in Fig. 12 and apparently all the parameters increase with a power of 3 to 4 with relative density in the considered range of the relative density.

## 4 Discussions

Natural snow at a temperature of approximately  $-8\text{ }^{\circ}\text{C}$  and a relative humidity of around 88% was filled into the PMMA tubes. Subsequently, the snow samples were tested at approximately  $-18\text{ }^{\circ}\text{C}$ . To ensure a suitable density range for the later stages of the  $\mu\text{CT}$  test and image processing, the filling was done without external compaction or with some compaction to achieve higher relative densities. Uniaxial compaction tests were conducted on the snow samples, yielding data covering a relative density range of approximately 0.17–0.39. The sample size was chosen to be as large as possible within the limits of the CT machine dimensions, and not that small to ensure grain independence. Thus, a tube with a diameter of 9 mm and a height of 11 mm was selected. Strain localization can occur even in initially homogeneous snow samples while undergoing homogeneous deformation. This strain localization has been demonstrated using the DVC, at least for strain rates in the ranges of  $10^{-3}$  to  $10^{-2}$  1/s [2], which is higher than the strain rate in this study ( $4.4 - 6.6 \times 10^{-4}$ 1/s).

**Fig. 12** Experimental (blue points) and Estimated (dashed lines) material constants,  $\eta_K$ ,  $E_K$ ,  $\eta_M$ , and  $E_M$ , using Burgers model as a function of snow density



The Young's modulus of snow can be estimated by analyzing the tangent line on the stress–strain curve shown in Fig. 10. This estimation is performed at various strains to determine the density-dependent modulus. It should be noted that this is an apparent modulus, as explained in [19], due to the viscoelastic nature of snow with unique mechanical properties. Thus, models that account for viscous effects, such as Burger's model, may be more appropriate. Nevertheless, the obtained modulus was found to be smaller than those reported by other researchers [12, 26]. This difference is attributed to the non-bonded nature of the snow tested in this study and the low effects of sintering, given the  $-18\text{ }^{\circ}\text{C}$  temperature during the experiments.

The stress-time response was utilized to estimate the viscoelastic material properties of natural snow. The Kelvin–Voigt model, commonly used in snow mechanics, consists of two connected parts: Kelvin and Voigt. In this study, four parameters, including modulus and viscosity, were estimated for both parts of the model, and their dependency on density was determined.

The strain distribution obtained from the DVC analysis indicated that normal strains exhibited localized behavior, typical of granular materials. The compressive normal strain reached approximately 0.33 or 0.25 for snow belonging to test 1 or test 2, respectively, as depicted in Figs. 8 and 9.

The shear strain also exhibited significantly higher localized values.

In line with the work of Mellor [19] and Shapiro [26], the viscosity was decomposed into “axial” and compactive terms, with the former being equivalent to the Maxwell viscosity in the four-parameter (Burgers) viscoelastic model.

## 5 Conclusions

Understanding the mechanical behavior of natural snow is valuable in different fields, like cold region engineering or polar studies. Here, we demonstrated a methodology to map the density-dependent material properties of natural snow by combining Burger's visco-elastic model and data obtained from step-wise uniaxial compression tests to identify the density-dependent material properties of natural snow. We also imaged the three-dimensional (3D) structure of the snow using  $\mu\text{CT}$  after each loading step at a temperature of  $-18\text{ }^{\circ}\text{C}$ , with a constant rate of deformation ( $0.2\text{ mm/min}$ ). The relative density of the snow increases from 0.175 to 0.39. The estimated modulus and viscosity terms, obtained from Burger's model, increase with the density of snow. The values of the Maxwell and



Kelvin–Voigt moduli range from 0.5 to 14 MPa and from 0.1 to 0.8 MPa, respectively. Meanwhile, the viscosity values for the Maxwell and Kelvin–Voigt models vary from 0.2 to 2.9 GPa-s, and 0.2–2.3 GPa-s, respectively, within the considered density range. These values exhibit an exponent of around 3.2 and 3.5 for Kelvin–Voigt and Maxwell modulus, respectively, when represented as power functions. The results of DVC show that, under the natural snow exhibits a highly localized strain field. The methodology presented in this study can be further extended to consider snow behavior at different temperatures, loading rates, and sintering stages. Moreover, the statistical nature of the determined material parameters can be studied in more detail by testing more snow samples.

**Author contributions** HB: participated in conceptualization, experimental work in total including snow sampling and  $\mu$ CT, conducted DVC, conducted material parameters extraction, and wrote the original manuscript. HL: participated in  $\mu$ CT scanning, proof reading, and reviewing the manuscript. JC: co-supervised the project, participated in conceptualization, proof reading, and reviewing the manuscript. FF: participated in  $\mu$ CT scanning, helped in DVC and image analysis, proof reading, and reviewing the manuscript. MS: supervised the project, participated in conceptualization, proof reading, and reviewing the manuscript.

**Funding** Open access funding provided by Lulea University of Technology.

**Data availability** Data sharing not applicable to this article as no datasets were generated or analysed during the current study.

## Declarations

**Conflict of interest** The authors declare that they have no known competing financial interests or personal relationships that could have appeared to influence the work reported in this paper.

**Open Access** This article is licensed under a Creative Commons Attribution 4.0 International License, which permits use, sharing, adaptation, distribution and reproduction in any medium or format, as long as you give appropriate credit to the original author(s) and the source, provide a link to the Creative Commons licence, and indicate if changes were made. The images or other third party material in this article are included in the article's Creative Commons licence, unless indicated otherwise in a credit line to the material. If material is not included in the article's Creative Commons licence and your intended use is not permitted by statutory regulation or exceeds the permitted use, you will need to obtain permission directly from the copyright holder. To view a copy of this licence, visit <http://creativecommons.org/licenses/by/4.0/>.

## References

1. H. Bahaloo, F. Forsberg, J. Casselgren, H. Lycksam, M. Sjö Dahl, Mapping of density-dependent material properties of dry manufactured snow using  $\mu$ CT. *Appl. Phys. A* **130**(1), 1–11 (2024)
2. T.W. Barraclough, J.R. Blackford, S. Liebenstein, S. Sandfeld, T.J. Stratford, G. Weinländer, M. Zaiser, Propagating compaction bands in confined compression of snow. *Nat. Phys.* **13**(3), 272–275 (2017)
3. B.K. Bay, Methods and applications of digital volume correlation. *J. Strain Anal. Eng. Design* **43**(8), 745–760 (2008)
4. C. Bernard, G. Delaizir, J.-C. Sangleboeuf, V. Keryvin, P. Lucas, B. Bureau, X.-H. Zhang, T. Rouxel, Room temperature viscosity and delayed elasticity in infrared glass fiber. *J. Eur. Ceram. Soc.* **27**(10), 3253–3259 (2007)
5. A. Buljac, C. Jailin, A. Mendoza, J. Neggers, T. Taillandier-Thomas, A. Bouterf, B. Smaniotto, F. Hild, S. Roux, Digital volume correlation: review of progress and challenges. *Exp. Mech.* **58**(5), 661–708 (2018)
6. Y.S. Chae, Frequency dependence of dynamic moduli of, and damping in snow. *Phys. Snow Ice Proc.* **1**(2), 827–842 (1967)
7. C. Chandel, P.K. Srivastava, P. Mahajan, Micromechanical analysis of deformation of snow using x-ray tomography. *Cold Reg. Sci. Technol.* **101**, 14–23 (2014)
8. C. Coleou, B. Lesaffre, J.-B. Brzoska, W. Ludwig, E. Boller, Three-dimensional snow images by x-ray microtomography. *Ann. Glaciol.* **32**, 75–81 (2001)
9. M. Dogan, A. Kayacier, Ö.S. Toker, M.T. Yilmaz, S. Karaman, Steady, dynamic, creep, and recovery analysis of ice cream mixes added with different concentrations of xanthan gum. *Food Bioprocess Technol.* **6**, 1420–1433 (2013)
10. L.K. Eppanapelli, F. Forsberg, J. Casselgren, H. Lycksam, 3d analysis of deformation and porosity of dry natural snow during compaction. *Materials* **12**(6), 850 (2019)
11. F. Forsberg, M. Sjö Dahl, R. Mooser, E. Hack, P. Wyss, Full three-dimensional strain measurements on wood exposed to three-point bending: analysis by use of digital volume correlation applied to synchrotron radiation micro-computed tomography image data. *Strain* **46**(1), 47–60 (2010)
12. B. Gerling, H. Löwe, A. van Herwijnen, Measuring the elastic modulus of snow. *Geophys. Res. Lett.* **44**(21), 11–088 (2017)
13. H. Han, M. Yang, X. Liu, Y. Li, G. Gao, E. Wang, Study on the constitutive equation and mechanical properties of natural snow under step loading. *Water* **15**(18), 3271 (2023)
14. H. Jellinek, R. Brill, Viscoelastic properties of ice. *J. Appl. Phys.* **27**(10), 1198–1209 (1956)
15. M. Kern, P. Bartelt, B. Sovilla, O. Buser, Measured shear rates in large dry and wet snow avalanches. *J. Glaciol.* **55**(190), 327–338 (2009)
16. R. Lakes, R.S. Lakes, *Viscoelastic materials* (Cambridge University Press, 2009)
17. K.G. Libbrecht, The physics of snow crystals. *Rep. Prog. Phys.* **68**(4), 855 (2005)
18. T. Mede, G. Chambon, P. Hagenmuller, F. Nicot, Snow failure modes under mixed loading. *Geophys. Res. Lett.* **45**(24), 13–351 (2018)
19. M. Mellor, *A review of basic snow mechanics* (US Army Cold Regions Research and Engineering Laboratory Hanover, 1974)
20. B. Pinzer, M. Schneebeli, T. Kaempfer, Vapor flux and recrystallization during dry snow metamorphism under a steady temperature gradient as observed by time-lapse micro-tomography. *Cryosphere* **6**(5), 1141–1155 (2012)
21. P. A. Prieto-Muñoz, H. M. Yin, and R. B. Testa, Mechanics of an adhesive anchor system subjected to a pullout load. II: Viscoelastic analysis. *J. Struct. Eng.* **140**(2):04013053 (2014)
22. B. Reuter, M. Proksch, H. Loewe, A. van Herwijnen, J. Schweizer, Comparing measurements of snow mechanical properties relevant for slab avalanche release. *J. Glaciol.* **65**(249), 55–67 (2019)
23. B. Salm, Mechanical properties of snow. *Rev. Geophys.* **20**(1), 1–19 (1982)
24. C. Scapozza, *Entwicklung eines dichte-und temperaturabhängigen Stoffgesetzes zur Beschreibung des visko-elastischen Verhaltens von Schnee*. Number 15357. vdf Hochschulverlag AG (2004)

25. M. Schneebeli, Numerical simulation of elastic stress in the microstructure of snow. *Ann. Glaciol.* **38**, 339–342 (2004)
26. L. H. Shapiro, J. B. Johnson, M. Sturm, and G. L. Blaisdell, Snow mechanics: review of the state of knowledge and applications. (1997)
27. M.N. Shenvi, C. Sandu, C. Untaroiu, Review of compressed snow mechanics: testing methods. *J. Terramech.* **100**, 25–37 (2022)
28. K. Shinojima, Study on the visco-elastic deformation of deposited snow. *Phys. Snow Ice: Proc.* **1**(2), 875–907 (1967)
29. C. Sigrist. *Measurement of fracture mechanical properties of snow and application to dry snow slab avalanche release*. PhD thesis, ETH Zurich (2006)
30. P.K. Srivastava, C. Chandel, P. Mahajan, P. Pankaj, Prediction of anisotropic elastic properties of snow from its microstructure. *Cold Reg. Sci. Technol.* **125**, 85–100 (2016)
31. M. Stoffel, P. Bartelt, Modelling snow slab release using a temperature-dependent viscoelastic finite element model with weak layers. *Surv. Geophys.* **24**(5), 417–430 (2003)
32. A. Van Herwijnen, J. Gaume, E.H. Bair, B. Reuter, K.W. Birke-land, J. Schweizer, Estimating the effective elastic modulus and specific fracture energy of snowpack layers from field experiments. *J. Glaciol.* **62**(236), 997–1007 (2016)
33. X. Wang, I. Baker, Observation of the microstructural evolution of snow under uniaxial compression using x-ray computed microtomography. *J. Geophys. Res.: Atmos.* **118**(22), 12–371 (2013)
34. A. Wautier, C. Geindreau, F. Flin, Linking snow microstructure to its macroscopic elastic stiffness tensor: a numerical homogenization method and its application to 3-d images from x-ray tomography. *Geophys. Res. Lett.* **42**(19), 8031–8041 (2015)
35. R.W. Webb, A. Marziliano, D. McGrath, R. Bonnell, T.G. Meehan, C. Vuyovich, H.-P. Marshall, In situ determination of dry and wet snow permittivity: improving equations for low frequency radar applications. *Remote Sens.* **13**(22), 4617 (2021)
36. C. Willibald, S. Scheuber, H. Löwe, J. Dual, M. Schneebeli, Ice spheres as model snow: tumbling, sintering, and mechanical tests. *Front. Earth Sci.* **7**, 229 (2019)

**Publisher's Note** Springer Nature remains neutral with regard to jurisdictional claims in published maps and institutional affiliations.